Spin Logic via Controlled Correlation in Nanomagnet–Dirac-Fermion Heterostructures

Xiaopeng Duan, Yuriy G. Semenov, and Ki Wook Kim*

Department of Electrical and Computer Engineering, North Carolina State University, Raleigh, North Carolina 27695-7911, USA

(Received 28 April 2014; revised manuscript received 15 August 2014; published 9 October 2014)

A hybrid structure combining the advantages of a topological insulator (TI), dielectric ferromagnet (FM), and graphene is investigated to realize the electrically controlled correlation between electronic and magnetic subsystems for low-power, high-functional applications. Two-dimensional Dirac-fermion states provide an ideal environment to facilitate strong coupling through the surface interactions with proximate materials. The unique properties of FM-TI and FM-graphene interfaces make it possible for active "manipulation" and "propagation," respectively, of the information state variable based solely on the spin logic platform through electrical gate biases. Our theoretical analysis verifies the feasibility of the concept for logic application with both current-driven and currentless interconnect approaches. The device and circuit characteristics are also examined in realistic conditions, suggesting the desired low-power performance with the estimated energy consumption for COPY or NOT operations as low as the attojoule level.

DOI: 10.1103/PhysRevApplied.2.044003

I. INTRODUCTION

Efficient electrical control of magnetic or spin states has long been desired for low-power and highly functional logic and memory devices [1,2]. Furthermore, the ability to propagate the magnetization states is also crucial, as the information must cascade through the system architecture. Traditionally, conversion to electrical signal has been used for the latter purpose by taking advantage of the conductance variation via the magnetoresistive or spin-valve effect (see, for instance, the Datta-Das transistors and the initial proposals on the magnetic tunnel-junction logic [3–5]). However, this approach encounters obvious drawbacks, such as the limited contrast in the output currents stemming from the inherent mismatch between two physical subsystems. It is instead advantageous to directly transfer the magnetization states through the natural magnetic or spin excitation without undergoing multiple transformations between the electrical and magnetic signals [6–10]. Accordingly, the recent effort in the magnetic or spin architecture focuses on the magnetic interaction between the adjacent functional cells for local operations (within the relaxation length), while a repeater cell or limited charge-magnetization conversion is considered for longer-distance on-chip communication [11–14]. A number of device concepts have been proposed, ranging from simple logic gates to specialty applications such as biomimetic elements, with a varying degree of success [15–17]. Physical mechanisms or systems that enable efficient manipulation and propagation of magnetization states remain the key for successful development of spintronics in the search for postsilicon technology.

The topological insulator (TI) and graphene offer a unique opportunity in this regard with each representing an extreme: spin manipulating and spin conserving, respectively [18–20]. The TI surface electron states are topologically protected, in which the spin is locked to the momentum. As a result, its surface state is sensitive to magnetic exchange interactions that break the time-reversal symmetry [19]. In fact, the anticipated alteration of electronic structures has recently been observed on the Fe- or Cr-doped Bi_2Se_3 surfaces both experimentally and by first-principles calculations [21–24]. Thus, the interdependence between the TI surface transport properties and the proximate magnet magnetization is readily predictable at room temperature [25–27]. In comparison, graphene has extremely weak spin-orbit coupling; the spin and the momentum can be treated as two independent quantum numbers, and the spin relaxation length can reach several microns [20]. Yet, the two-dimensional nature of the graphene crystal enables strong surface interaction with a proximate ferromagnet (FM) that can induce electron spin polarization [28–30]. The linear dispersion relation of graphene electrons also indicates that the induced spin polarization can be controlled electrostatically [31].

Hence, the combination of a TI, nanomagnet, and graphene has ideal qualities to meet the two major requirements of logic device design mentioned earlier: (i) manipulation of the desired information state variable (i.e., magnetization) by electrostatic control at the TI-FM interface and (ii) robust propagation of information via the (FM-induced) spin polarization in the graphene interconnect. As no lattice displacement is involved, no risk of structural instability exists in contract to normal strain-based multiferroic materials. Moreover, dynamical control of magnetic susceptibility and consequent logic

*kwk@ncsu.edu

reconfiguration offered by Dirac fermions [31] is difficult to be matched in the metal-based spin circuits.

In this paper, such a logic device is put forth and evaluated in detail by taking advantage of the controlled correlation between a magnet and the adjacent TI and graphene layers; i.e., the magnetization affects the TI and graphene electronic states and vice versa. Section II outlines the overall operating principles utilizing the Bennett clocking scheme. Two approaches for information transfer between adjacent cells are formulated and modeled in Sec. III, followed by the discussion on logic circuit in terms of a one-bit full adder (Sec. IV). The performance issues and the switching reliability at room temperature are also addressed (Sec. V), as the magnetic dynamics is sensitive to random thermal fluctuations.

II. SPIN LOGIC OPERATION PRINCIPLES

The unit cell of the proposed spin logic consists of a FM-TI stack placed on top of the graphene channel as shown in Fig. 1(a). The top and bottom gate electrodes are separate from the active region by a thin dielectric, respectively. The FM is assumed to be insulating or dielectric such as $Y_3Fe_5O_{12}$ or Fe_7Se_8 [32]; the metallic magnets could cause unintended changes in the TI surface electron density and, thus, are not desirable. The interface between the FM and the TI is used to locally control the magnet, while that between the FM and the graphene channel supports the means of interconnect. More specifically, the information is encoded in the magnetization orientation of the magnet, which is then transferred to the electron spin polarization in the graphene layer for dissemination. A functional combination of these two interfaces with the information-carrying FM in the middle enables straightforward implementation of Bennett clocking.

The Bennett clocking [Fig. 1(b)] refers to the magnetic switching scheme that uses one clock to put the magnetization in a neutral state (the null stage) and another clock to apply the signal that generates a small tilt to determine the final state (the active stage) [34,35]. If the first clock that overcomes the barrier is applied electrostatically and the critical signal in the absence of the barrier is small, this scheme is expected to offer very low energy consumption. Further, it could also ease the requirement on the signal-to-noise ratio for reliable performance. In the present device, the first stage of Bennett clocking is achieved electrically by applying a proper bias at the top gate as reported in Ref. [33]. Because of the exchange interaction between the TI and the magnet, the band structure of the TI surface electrons varies according to the magnetization and so does the system free energy. More specifically, the free-energy landscape of the combined system prefers the magnetization to be in the out-of-plane configuration as it induces a band gap at the Dirac point. Adding the fact that the strength of this "preference" is dependent strongly of the Fermi level on the TI surface, the 90° magnetization

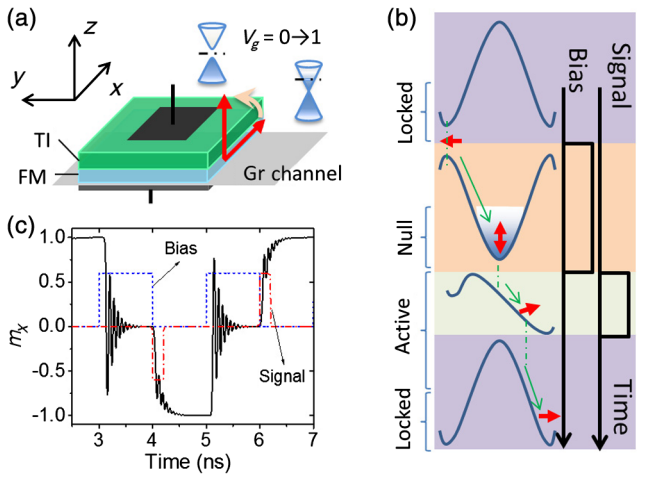

FIG. 1. (a) Schematic illustration of the basic component that consists of a two-layer structure of TI and FM plus the control gates. With the gate bias, an effective out-of-plane anisotropy can be induced in the magnetic layer that rotates the magnetization by 90° from the in-plane orientation [33]. The graphene (Gr) channel interconnects the elemental cells. While not shown explicitly, note that the top and bottom gate electrodes are separated from the active region by a thin dielectric, respectively. (b) In the Bennett clocking scheme, the bias-induced energy minimum constitutes the neutral state, where the system resides at the end of the biasing stage (Null). A signal pulse applied subsequently provides an additional effective magnetic field to tilt the free-energy landscape (Active). The arrows indicate evolution of the magnetization in the ideal conditions. After the relaxation, the magnetization is locked to a stable state along the easy axis. (c) Snapshot of the magnetization evolution for 180° switches with Bennett clocking in the time domain (represented by m_x). Bias on the TI gate and signal pulses through the channel are indicated by the dashed lines.

rotation from the in-plane easy axis of the magnet to the vertical direction can be achieved by manipulating the gate bias. It constitutes the neutral state in the Bennett clocking scheme once the bias is withdrawn (i.e., the null stage). Then, spin-polarized electrons in the graphene channel can provide the second effective magnetic field that tilts the magnetization slightly toward the desired relaxation direction (i.e., the active stage). The durations of bias and signal pulses are typically of the order of 1 ns and its fraction, respectively, as shown in Fig. 1(c). The minimum pulse length depends on the material properties and thermal noise.

To output the information, the insulating magnet adopted in the design cannot directly inject polarized electrons into the interconnect medium, as it does not have free carriers. Instead, the controllable surface exchange interaction at the FM-graphene interface offers an alternative mechanism to induce a spin-dependent behavior in graphene that supports transmission of spin information. Specifically, two types of operations are possible: one with and the other without the involvement of electrical current flow. The first scheme

relies on the spin-dependent carrier transport induced by the exchange barrier at the FM-graphene interface, while the other takes advantage of a graphene electron-mediated coupling between the adjacent magnets. The corresponding physical accounts for each outlined dynamics are detailed in the following sections.

Before proceeding with the specifics, it is important to note that the proposed device is intended for room-temperature operation. This is possible since the spin-momentum interlock—the essential feature of the TI—is not limited to low temperatures. At the same time, the concern of thermal phonon excitation on the topological phase (i.e., the inelastic carrier-phonon interaction) is of no relevance because the envisioned functionality does not rely on the carrier transport characteristics of the TI surface states. The bulk band gap of a typical TI (e.g., approximately 0.3 eV for Bi_2Se_3) can also be sizably larger than the ambient thermal energy. In fact, the earlier theoretical analysis has already illustrated the desired correlation between the TI electronic states (Bi_2Se_3 as in the current study) and a proximate magnet in the presence of thermal broadening at 300 K [33]. Similarly, the performance on the graphene side of the structure can meet the room-temperature condition due to the relatively long spin relaxation time and length as mentioned above.

III. INFORMATION TRANSFER BETWEEN ADJACENT CELLS

For an efficient spin logic implementation, it is preferred that the information is transferred in the form of electron spin polarization to avoid the intrinsically inefficient conversion to the electric current. One constraint, however, is the limited distance for reliable signals, which is set by the spin relaxation length. As such, transmission of the information is often accomplished in a cascade, where the state propagates cell by cell along the path. Thus, the issue of information transfer is essentially the interaction between the adjacent cells. At the same time, it is highly desirable if both duplication (COPY) and inversion (NOT) operations of the upstream spin state can be realized in each of the cascading stages with a relatively simple control and layout arrangement. These are the underlying principles that motivate the adopted approaches.

A. Via spin-polarized electrical currents

The concept of information transfer based on the spin-polarized electric current is shown in Fig. 2(a), where the state of magnetization $\mathbf{M}_2$ is determined by $\mathbf{M}_1$ in the Bennett clocking. Through the exchange interaction with $(\mathbf{M}_1 \| \hat{\mathbf{x}})$, the graphene band structure in the upstream cell lifts the spin degeneracy. Thus, the incoming electrons from the left experience different potential barriers for the spin states parallel and antiparallel to $\mathbf{M}_1$, giving rise to a spin-dependent conductance. The transmission probability

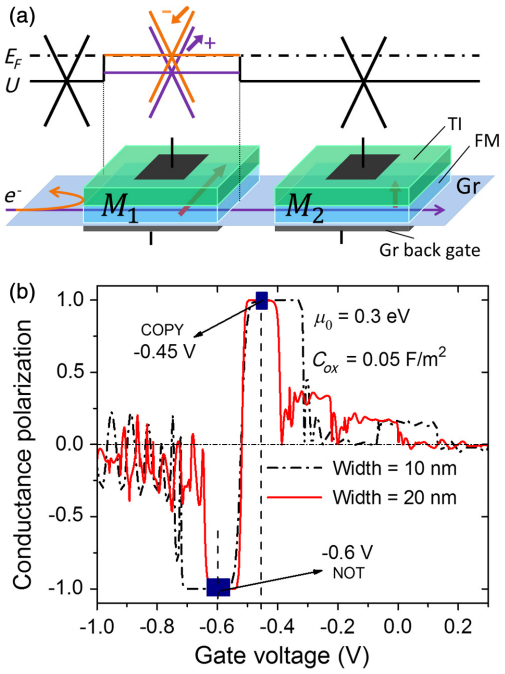

FIG. 2. (a) COPY/NOT connection of two unit cells. The surface exchange interaction with the magnet induces a spin-dependent barrier in graphene. By controlling electron transmission through the spin-split bands (via the back-gate bias at $\mathbf{M}_1$), spin polarization of electrons arriving at $\mathbf{M}_2$ can be selected. (b) Calculated conductance polarization in the graphene interconnect as a function of gate voltage. The high-polarization windows are marked by the filled rectangles.

depends on the quantum state of electrons that induces Klein tunneling. The resulting expression, when an electron of energy E in the graphene channel encounters a potential barrier of U_g, is found to be [28]

$$T = \frac{(\xi^2 - u^2)(1 - u^2)}{(\xi^2 - u^2)(1 - u^2) + u^2(1 - \xi)^2 \sin^2(k_F L \sqrt{\xi^2 - u^2})}, \tag{1}$$

where $\xi = (E - U_g)/E$ and $u = k_x/k$ ($k = \frac{|E|}{\hbar v_F}$, the magnitude of wave vector $\mathbf{k}$). In addition, the transverse wave vector (k_y) is quantized in a narrow channel and expressed as $k_y = (n + 1/2)\pi/W$, where W is the channel width, and the integer quantum number n is confined within $[0, \frac{kW}{\pi} - \frac{1}{2}]$. Considering the contribution from multiple energy levels at a finite temperature and the valley degeneracy $g_v = 2$, the conductance of one spin channel is calculated in the Landauer-Büttiker formalism as

$$G(E_F, U_g) = g_v \frac{e^2}{\pi h} \int_{-\infty}^{\infty} dE \sum_n T(n, E, U_g) \left[-\frac{\partial f(E, E_F, T)}{\partial E} \right], \tag{2}$$

where $f(E, E_F, T)$ is the Fermi-Dirac distribution.

The signal strength is determined by the spin polarization of the conductance [Fig. 2(b)], which is defined as the ratio of the difference between the two spin channel conductances over the total conductance. The quantization step determined by the adopted extreme quantum limit ($=\pi\hbar v_F/W$) is approximately 0.2 and 0.1 eV for the channel width of 10 and 20 nm, respectively [36], sufficiently large even for room temperature. The conductance approaches zero when the bias depletes the channel including the $n=0$ state. Because of the spin splitting by the adjacent magnet, the antiparallel spin state becomes depleted ahead of the parallel state in the conduction band, while the opposite is the case for the valence band. The consequence, thus, opens two windows for large polarization with opposite signs. This means that the polarization can be chosen to be either parallel or antiparallel to input magnetization $\mathbf{M}_1$ by a simple switch of the applied potential, achieving the desired COPY and NOT operations between two neighboring cells with electrical control as shown in Fig. 2(b).

In the numerical calculation, the magnets are assumed to possess identical properties with the size of $60\times60\times2$ nm^3, saturation magnetization $|\mathbf{M}_i|=160$ Oe, intrinsic magnetic anisotropy of 40 fJ/μm^3 along the in-plane hard axis (e.g., y), and a damping factor of 0.1. The exchange-coupling energy is taken to be 40 meV at both the TI-FM and the FM-graphene interfaces [33], inducing spin splitting of 80 meV for the spin-dependent barrier. A relevant experimental report indicates the opening of a 0.12-eV band gap due to the magnetic doping on the TI surface, corresponding to an exchange constant around 60 meV [22]. Another measurement in the Ni-graphene-Ni structure shows the exchange field as large as 2000 Oe between the Ni layers, which results in an estimated exchange constant around 240 meV at the Ni-graphene interface [37]. Similar estimates have also been seen from the first-principles calculations [29,38]. While these are preliminary results and a direct measurement is still lacking, it is reasonable to anticipate the exchange constant to be in the tens to hundreds of meV at the well-prepared interfaces. As for the intrinsic chemical potential in graphene and the back-gate capacitance, they are set at 0.3 eV and 0.05 F/m^2, respectively. The signal current on the graphene channel also assumes the strength of 0.1 μA/nm. These parameters are used hereafter unless explicitly specified otherwise.

One potential concern for this scheme based on the spin-polarized current is the backward propagation of information, i.e., how to ensure that the spin-polarized electrons flow only downstream. This can be addressed by patterning the graphene interconnect to separate the input and output channels as indicated in Fig. 3. The output of the upstream cell is connected to the input in the downstream, forming an electron path indicated by the red curved arrow, where only the cells in the two neighboring stages are connected at a time. The asymmetric pattern with a wider input channel is to maximize the area of exchange interaction with the target magnet. For the fan-out, multiple cells can be placed along the same input channel to share the input, whose capacity is limited by electron spin relaxation. Given a typical relaxation length of 4 μm in graphene [20], the upper limit may approach approximately 40. According to the reliability analysis discussed in Sec. V, the energy consumption for each COPY or NOT operation could be of the order of femtojoules that is dominated by the Joule heating from the signal current.

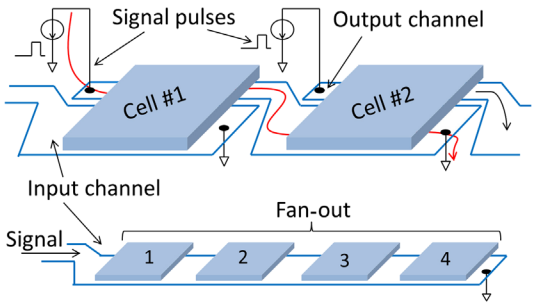

FIG. 3. Separate input and output channels are defined for the information flow. The red curved arrow indicates the electron path between two neighboring cells. The fan-out is realized by placing multiple target cells along the same input channel.

B. Via electron-mediated exchange interactions

In contrast to the above approach, a fully electrostatic mechanism can eliminate the Joule heating and, thus, reduce the power requirement. As mentioned earlier, the magnetic susceptibility of graphene electrons can be modulated by a gate bias—a consequence of the linear dispersion relation [31]. This brings an opportunity to electrostatically turn on and off the effective exchange coupling between adjacent magnets that is mediated by the graphene electrons in the channel. As shown in Fig. 4, an electron potential well can be generated by the graphene back gate to facilitate the overlap of electron wave functions between the two involved cells. Qualitatively speaking, the upstream cell with a stable magnetization state ($\mathbf{M}_1\|\pm\hat{\mathbf{x}}$) will induce electron spin polarization in the graphene channel that diffuses to the downstream cell. With negligible decay over the device dimension [20], this aligns the target cell to realize the COPY operation [Fig. 4(a)]. On the other hand, insertion of a control magnet ($\mathbf{M}_C\|\pm\hat{\mathbf{y}}$) in the middle (magnetized normal to $\mathbf{M}_1$) will cause spin precession as indicated in Fig. 4(b). If its length is such that the spin experiences a 180° rotation when reaching the target cell, the antiparallel alignment can be achieved for the NOT operation. The required distance for a π turn can be estimated as $L_C=\pi\hbar v_F/2G_0\approx26$ nm following the analysis described in an earlier study (with $G_0=40$ meV as specified above) [39]. Note that the

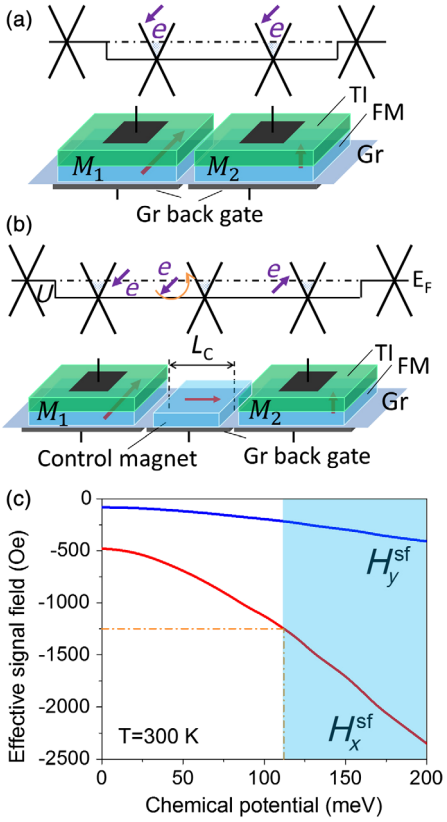

FIG. 4. (a) COPY and (b) NOT operations in the currentless approach that are achieved via electrostatically controlled coupling between magnets when the downstream cell is in the active state. An energy well can be introduced by simultaneously applying a bias to the graphene back gates. The gap between the gates can be ignored so long as it is smaller than the screening length which is typically several tens of nanometers in graphene. (c) Effective signal field exerted on the downstream cell as a function of chemical potential in the graphene channel. The shaded region indicates the condition for error rate below 10^{-6}.

obtained L_C is well within the electron spin mean free path in graphene.

The strength of the electron-mediated coupling effect can be obtained by considering the induced change in the free energy of the system. For instance, the thermodynamic potential of graphene electrons is a function of magnetic states as

$$E_c(\mathbf{m}_1,\mathbf{m}_2) = -k_BT\sum_{b,k}\ln\left\{1+2\frac{\exp\left(\frac{E_F-E_{b,k}}{k_BT}\right)}{\left[1+\exp\left(\frac{E_F-E_{b,k}}{k_BT}\right)\right]^2}\times\left[\cosh\frac{\Delta_k(\mathbf{m}_1,\mathbf{m}_2)}{k_BT}-1\right]\right\}, \quad (3)$$

where E_F is the chemical potential, b ranges the conduction and valence bands, and $2\Delta_k(\mathbf{m}_1,\mathbf{m}_2)$ corresponds to spin splitting in the graphene band caused by the exchange interaction with the magnets. For convenience, the normalized magnetization vector (i.e., $\mathbf{m}_i = \mathbf{M}_i/|\mathbf{M}_i|$) is used as all magnets are assumed to have the same saturation magnetization. The expression clearly shows that the finite spin splitting always decreases the thermodynamic potential. Thus, the problem of finding the minimum $E_c(\mathbf{m}_1,\mathbf{m}_2)$ reduces to a search for the maximum energy splitting $\Delta_k(\mathbf{m}_1,\mathbf{m}_2)$. Subsequent calculations illustrate that the $\mathbf{m}_2 = \mathbf{m}_1$ state indeed provides the minimum E_c in Fig. 4(a) (COPY), while it is a state near $\mathbf{m}_2 = -\mathbf{m}_1$ in Fig. 4(b) (NOT) [40].

The dependence of the free energy on the magnetization of the target cell ($\mathbf{M}_2$) may be best interpreted in terms of an effective field that determines its stable state. Adopting an approach commonly used in the magnetic system, the macroscopic field may be obtained as $\mu_0\mathbf{H}^{sf} = -\frac{1}{V_2}\partial E_c/\partial\mathbf{M}_2$ (where V_2 is the volume of the target magnet and μ_0 the permeability constant) that formally defines the orientation and strength of the spin signal. Figure 4(c) shows the calculated outcome for the NOT gate configuration ($L_C = 26$ nm) as a function of E_F. The presence of both x and y components indicates that the energy minimum occurs slightly away from the antiparallel $\mathbf{m}_2 = -\mathbf{m}_1$ state. Nonetheless, the carrier-mediated exchange interaction achieves inversion of the spin signal (i.e., polarization) as desired. The observed enhancement of the signal strength with E_F ensures a robust performance against thermal noise with an applied back-gate bias. For instance, H^{sf} of approximately 1250 Oe can realize the error rate below 10^{-6} (see Sec. V for a more detailed discussion). The necessary shift of 0.1 eV in E_F from the Dirac point translates to the back-gate voltage swing of about 0.12 V. The corresponding energy requirement is approximately 10 aJ per COPY or NOT operation including the amount needed to prepare the target cell in the Bennet clocking scheme. Moreover, with only capacitor charging and discharging, a significant portion of this energy can be recovered in the clock network [41]. Accordingly, the net consumption may be reduced to the attojoule level. In this scheme, it is advantageous to have an intrinsically depleted graphene channel unlike the mechanism based on the spin-polarized current.

IV. CONSTRUCTION OF LOGIC CIRCUITS

Once the elemental cell and the cell-to-cell COPY and NOT operations are established, the rest of the Boolean logic can be built on the spin logic platform with majority gates [9,10,42–44]. We demonstrate the logic realization with a one-bit full adder. It is important to note that the one-bit adder logic can be decomposed to two majority logic components: the carry-out bit (C_{out}) is the majority gate of inputs a,b,c, and the sum bit (S) equals a five-input majority logic of a, b,c, and two $\overline{c_{out}}$'s [40].

Following the spin-current-based interconnect scheme (Sec. III A), Fig. 5(a) shows a one-bit adder layout to accomplish the two-stage operations. In the first stage,

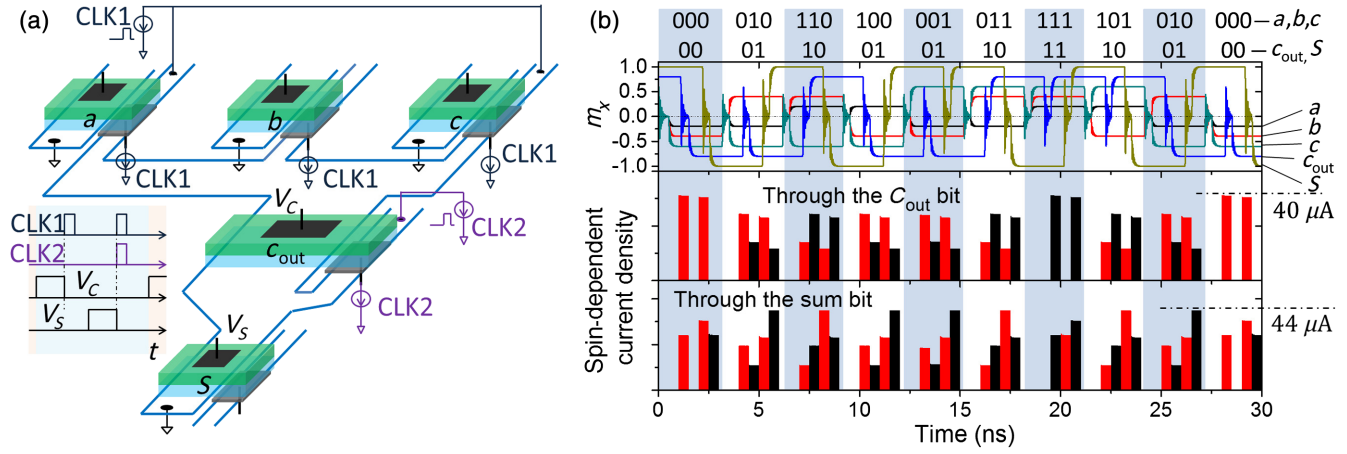

FIG. 5. (a) Circuit layout of a one-bit full adder. The insert shows the clocks and control signals. The graphene back-gate biases and the channel inputs share the same clock but may differ in values. A doubled strength of the outgoing signal from C_{out} (specifically, $\overline{c_{out}}$) can be achieved by adjusting the cell size or the channel driving voltage. (b) Results of ten add operations performed with the input states set dynamically in the simulation. The top panel shows the magnetization of each cell, and the bottom two provide the spin parallel ($\hat{\mathbf{x}}$, black) and spin antiparallel ($-\hat{\mathbf{x}}$, red) currents through the input channels of C_{out} and S, respectively. The magnetization m_x varies between 1 and -1 in all five cases (e.g., $m_x = \pm 1$ for logic "1" and "0," respectively). The heights are adjusted artificially to distinguish the curves from each other for easier viewing (top panel). Similarly, the spin antiparallel current is artificially shifted to the left by 0.5 ns to separate it from the spin parallel current (bottom panels).

electrons are injected by clock CLK1 through a, b, c cells to set the state of C_{out}. The second stage includes another clock CLK2 to inject electrons through the output channel of C_{out} (the narrow channel) with the reversed polarization (i.e., $\overline{c_{out}}$). Doubling the $\overline{c_{out}}$ signal can be achieved by either adjusting the cell size or increasing the driving voltage in the corresponding output channel. At the circuit level, each unit acts as a set of resistors, and the circuit energy consumption scales with the logic complexity. We develop a fully coupled device-circuit simulation method [40] to verify the adder behavior with ten successive add operations that cover the truth table [Fig. 5(b)]. In this simulation, we assume that all the magnets have the same parameters as previously stated, and the input and output channels are divided with a ratio of 4:1. The driving voltage is set to 0.3 V, except the output channel of C_{out} that is 0.45 V to double the signal strength. The back-gate voltages are chosen according to Fig. 2, i.e., -0.45 V for COPY and -0.6 V for NOT. As each stage of magnetization switching is achieved within the period of 1 ns, a total of 3 ns is needed for the one-bit adder including the process to prepare the input states a,b,c. With the specified conditions, the total channel current is around 30–80 μA, and the corresponding energy consumption is approximately 15 fJ.

When the currentless operating mechanism is adopted (Sec. III B), on the other hand, construction of the logic circuits essentially amounts to arranging each elemental cell on a universal graphene sheet with properly clocked gates. It follows a different methodology compared to the current-based circuits. One characteristic is the compact layout required by the nature of local exchange interactions (such as the spin relaxation length and the gate-field screening effect) [20,45]. A tentative one-bit adder design is shown in Fig. 6 following the same two-stage operating procedure. In the first stage, CLK1 induces the electron wave-function overlap in the graphene channel between the input cells and output cell C_{out} to achieve a three-input majority gate. The next stage has CLK1 and CLK2 applied together to overlap all the cells for the equivalent five-input majority logic. The inserted control magnet inverts the signal from c_{out} to $\overline{c_{out}}$. In the actual implementation, however, this trial design may need adjustments, as it is based on the assumption that the outcome from our two-cell analytic prediction holds for the complex geometry, at least qualitatively.

V. MAGNETIC SWITCHING PERFORMANCE AND RELIABILITY

For a comprehensive evaluation of the proposed logic devices, it is important to characterize the switching dynamics and verify the robustness in a thermal bath. Particularly, the Bennett clocking scheme relying on two successive 90° magnetization rotations via a neutral state is inherently susceptible to the fluctuations that could limit not only the operation accuracy but also the switching speed. The well-established Landau-Lifschitz-Gilbert (LLG) equation is used to numerically examine these issues [40]. The investigation primarily considers the spin-current-based interconnect scheme with 100% polarization for simplicity. The performance of the electrostatic approach can also be understood by correlating the strength of the spin current to the induced effective magnetic field. In fact, this analysis may be applicable more broadly to

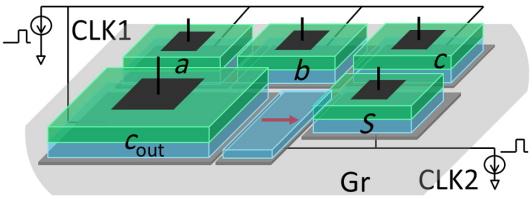

FIG. 6. Tentative circuit layout for the one-bit adder in the currentless approach. It uses the same control clocks and follows the two-stage operation as in the current-driven design.

other spin logic realizations that utilize similar operating principles.

A. Switching speed

As described in Sec. II, Fig. 1(c) illustrates a snapshot of switching with Bennet clocking. One particularly interesting parameter that warrants additional scrutiny is the hard-axis anisotropy K_y along the y axis, as it can significantly influence the details of rotational dynamics. The expectation is that the magnetization could switch and relax faster with a larger K_y since it tends to confine the switching path to the x-z plane. Our simulation of the first 90° rotation (with m_x changing from 1 to 0 via the top gate bias) indeed indicates that the desired operation can be achieved more quickly with the characteristic time shorter than 0.5 ns once K_y increases above approximately 20–30 fJ/μm^3. It should be noted that application of the hard-axis anisotropy in the y direction together with the demagnetization field amounts essentially to "the easy axis" along the x direction, which has been assumed by numerous studies in the literature [9,14]. Roughly speaking, the hard-axis anisotropy must be at least comparable to the demagnetization energy for the desired confinement effects on the switching dynamics.

The second half of the full 180° rotation is also improved by a larger hard-axis anisotropy as indicated in Fig. 7. Here, a continuous signal current instead of a pulse [i.e., Fig. 1(c)] is considered to drive the magnetization until it reaches the correct direction to capture the main features. Both the polarized current and the hard-axis anisotropy provide the driving force for relaxation, and the switching time drops when their values increase. At a small current density, the relaxation is mainly driven by the intrinsic anisotropy field so that the switching time varies significantly over different anisotropy values. As the current rises, the exchange torque also drives the switching process to reduce the switching time. When the current is high enough to dominate over the contribution from the anisotropy, the curves tend to converge (to approximately 0.1–0.2 ns). It is also worth noting that at a sufficiently large anisotropy (e.g., $K_y \gtrsim 50\,\mathrm{fJ}/\mu\mathrm{m}^3$), the influence of the signal amplitude becomes insignificant in the simulation range. The corresponding dashed lines indicate the energy consumption per ohm resistance. It shows a steep increase for switches with a high current even though the duration reduces. Accordingly, a large K_y appears to be generally favorable (i.e., for both fast switching and low energy consumption).

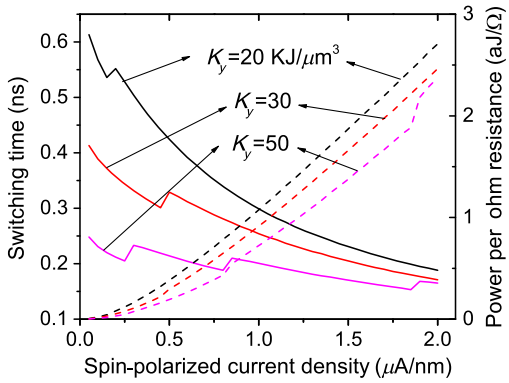

FIG. 7. Switching time (solid lines) and corresponding power consumption (dashed lines) of the current-driven relaxation process from $m_z = 1$ to $m_x = 1$ ($z \to x$). The relaxation is marked completed when $|m_x| > 0.9$. The power consumption per ohm is calculated as I^2t, where I is the total current assuming a 60-nm channel width and t is the duration of relaxation.

B. Possible error sources

In the magnetic switching process based on Bennett clocking, the switching errors are mainly caused by deviation from the neutral state (after the first 90° rotation) as well as the low-energy path leading to the energy minimum with unintended polarization. One such example is illustrated in Fig. 8 based on the magnetization phase-space analysis. As displayed by the white and green curves in Fig. 8(a), two states with nearly identical locations in the

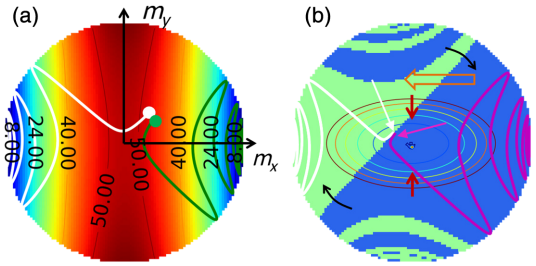

FIG. 8. Switching characteristics related to the operation error rates. (a) Intrinsic energy landscape of the magnet that drives the relaxation after the signal pulse. The green line shows a path along which the magnetization relaxes to the same side of the initial state, while the white one indicates that a low-energy valley can lead the magnetization to the opposite side. (b) Topology of switching success or failure with a signal current pulse of 0.2 ns at 0.2 μA/nm. The null-state magnetization that relaxes to $m_x = 1$ is shown in blue (success), while that leads to $m_x = -1$ is marked in green (failure). The white and purple curves provide two sample paths (with the arrows pointing to the starting locations). The dot in the middle indicates the magnetization distribution at the end of a 0.5-ns biasing stage. The ellipses indicate the lowest-energy contours with an increment of $2k_BT$ from the neutral state.

intrinsic free-energy landscape (close to the neutral $m_z = 1$) can end up with two drastically different relaxation paths to opposite polarizations. This can be attributed to the convolution and close entanglement in the high-energy regions in the context of precessional dynamics [46]. Evidently, the rotational nature of magnetization switch adds complexities to the problem. Increasing the signal intensity, while certainly helpful, is only part of the solution for the robust performance. Figure 8(b) summarizes the success and failure of the switching operation when a current pulse of 0.2 ns at 0.2 μA/nm is applied to set the final state to $m_x = 1$. The darker colored (blue) region represents the initial "null" states from which the magnetization relaxes to the desired final state with the aid of the signal current (i.e., $m_x = 1$; success), whereas the lighter region (green) results in the failure or error with the final polarization in the opposite direction ($m_x = -1$). An increased signal intensity moves the lighter/darker boundary towards the failure side (i.e., less failure; see the block arrow). The larger hard-axis anisotropy K_y, on the other hand, rotates the boundary clockwise (see the black arrows). Aside from the asymmetric pattern of the switching map, the concentric ellipses show the constant energy contours with an increment of $2k_BT$ from the neutral state. This gives a qualitative measure of random thermal fluctuation. For instance, the trouble spot in Fig. 8(b) is the lighter colored region within a given ellipse (leading to an error). In the present discussion, only the states with $m_z \geq 0$ are considered with its value determined by $\sqrt{1 - m_x^2 - m_y^2}$ in the 2D plot; the pattern for $m_z \leq 0$ satisfies the reflection symmetry.

To be more precise, two major sources can lead to the unintended spread in the null-state distribution after the initial 90° rotation, namely, insufficient relaxation and thermal fluctuations. The former will dominate only if the operating frequency is too high, while the latter always exists at the level of severity determined by the temperature. According to Sec. V A, the switching time to the neutral state (i.e., the first 90° rotation) is well within 1 ns (e.g., $\lesssim$0.5 ns), indicating that the insufficient relaxation can easily be avoided. The case of Fig. 8(b) clearly illustrates this point, where the applied bias of 0.5 ns sufficiently concentrates the distribution to the desired $m_z = 1$ state (see the tight distribution near the center). Consequently, the distribution of null-state magnetization in a well-designed operating condition is determined by thermal fluctuations, and errors will occur if the signal is not able to remedy all of the possible magnetization within this distribution including the added complexities in the precessional dynamics.

C. Error rate evaluation

The device robustness is closely related to the switching details. A conventional treatment to examine the performance in a realistic environment is to add a white thermal field to the LLG equation (i.e., the stochastic LLG equation) that induces a Brownian motion [47,48], i.e., $\mathbf{H}'_{\text{eff}} = \mathbf{H}_{\text{eff}} + \mathbf{H}_{\text{th}}$. The random thermal field $\mathbf{H}_{\text{th}}$ is described by a Gaussian distribution with the variance determined from the fluctuation-dissipation theorem:

$$\langle H^i_{\text{th}}(t_1) H^j_{\text{th}}(t_2) \rangle = \frac{2k_BT\alpha}{\mu_0 V M_0 \gamma} \delta_{i,j} \delta(t_1 - t_2), \qquad (4)$$

where V is the magnet volume and indices i, j correspond to the coordinate axes [47,49]. As mentioned, this term can be readily included in the calculation. One major difficulty of the stochastic approach, however, is that the number of the required simulations increases at least linearly with the desired accuracy. For instance, the simulations must be repeated 10^6 times or more in order to accurately estimate the error rate of 10^{-6} (i.e., one incorrect event out of 10^6 operations), not to mention the numerical complexities associated with various discretization issues in the actual implementation [50]. For an alternative, computationally more-efficient method, it is worth noting that the magnet is most vulnerable to a thermal fluctuation at the null state. Accordingly, we consider the thermal variation (or noise) explicitly through the null-state magnetization distribution, while the relaxation dynamics is treated deterministically based on the LLG equation. Then, the error rate P_s can be estimated as

$$P_s = 1 - \int_{m_z \geq 0} d\mathbf{m}_n R(\mathbf{m}_n) F(\mathbf{m}_n) \Big/ \int_{m_z \geq 0} d\mathbf{m}_n F(\mathbf{m}_n), \qquad (5)$$

where $F(\mathbf{m}_n)$ is the distribution of the null-state magnetization $\mathbf{m}_n$ and $R(\mathbf{m}_n)$ denotes the simulated switching result. More precisely, $R(\mathbf{m}_n) = 1$ if the operation results in the desired outcome and $R(\mathbf{m}_n) = 0$ for the error (or failure). Figure 9 shows the results of $R(\mathbf{m}_n)$ on the x-y plane for a number of cases. The plots clearly illustrate the earlier statement that the boundary between the failure and success regions moves towards the failure side when the signal current J increases and rotates clockwise when the hard-axis anisotropy K_y increases. As for $F(\mathbf{m}_n)$, we use a Boltzmann distribution to weigh each possible null-state magnetization, i.e., $F(\mathbf{m}_n) = \exp[-E_m(\mathbf{m}_n)/k_BT]$, where E_m represents the magnetic energy including the bias-induced out-of-plane anisotropy. This choice can be justified since the thermal fluctuations would be dominant over the variation by insufficient initial relaxation under proper operating conditions (see the discussion in Sec. V B). Of the isoenergy contours plotted in Fig. 9, it is interesting to note that nearly 90% of the thermal distribution is contained in the first $2k_BT$.

The calculated error rates are shown in Fig. 10 as a function of in-plane hard-axis anisotropy, magnet size, signal pulse duration, and the strength. From the results, it

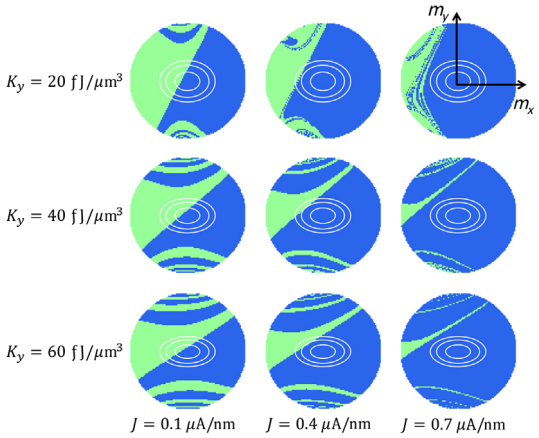

FIG. 9. Topology of switching success/failure with a signal current pulse of 0.4 ns in duration at different values of strength J and anisotropy K_y. The null-state magnetization that relaxes to $m_x = 1$ is shown in blue (success), while that which leads to $m_x = -1$ is marked in green (failure). The magnet has a dimension of $60 \times 60 \times 2$ nm^3. The ellipses indicate the energy contours of 2, 4, and $10k_BT$ from the neutral state.

is evident that the device can reach the desired high degree of robustness once the hard-axis anisotropy becomes sufficiently large. In fact, K_y above approximately 20–30 fJ/μcm^3 appears to converge without a large deviation between the different values. Accordingly, the threshold current density for a target error rate (say, 10^{-4}–10^{-6}) is expected to be relatively insensitive to this crucial parameter [see Figs. 10(a) and 10(b)]. When the magnet size increases, the switching becomes generally more reliable; this can be attributed to the larger surface area enabling a stronger interaction with the signal current. In the case of signal pulse duration, it shows a dependence akin to that of K_y. As can be seen from Fig. 10(c), the proposed device provides very comparable performance once the signal pulse is approximately 0.2 ns or longer. One key difference is that the error rate may exhibit a threshold behavior on the duration. Namely, there may be a minimum pulse length below which the operation cannot attain high fidelity even with an increase in the signal current strength (see, for example, the case of 0.1 ns). The requirement on the pulse duration may be partly compensated by a larger in-plane hard-axis anisotropy. Figure 10(d) illustrates the point clearly, where the performance of the 0.1-ns case converges to an error rate similar to those of the longer pulses as the anisotropy energy increases beyond the demagnetization terms. An additional finding of interest in Fig. 10(d) is that the error rates for the longer pulses ($\gtrsim$0.4 ns) seem to reach the minimum at around $K_y =$ 20 fJ/μm^3 and then rise afterward with a converging trend in the end. This can be understood by examining the

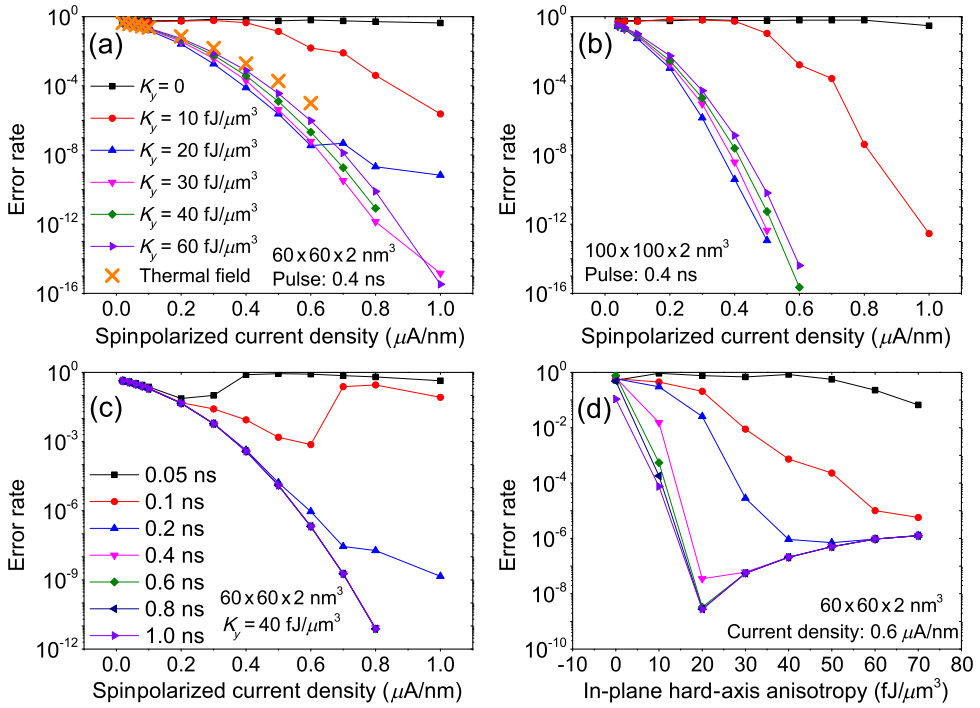

FIG. 10. Variation of the switching error rate over magnet size, signal current duration, signal current density, and hard-axis anisotropy. Identical line colors and symbols are used in (a) and (b) to denote different values of K_y, whereas (c) and (d) share the same notation on the pulse duration. In (c), the curves for duration over 0.4 ns essentially overlap each other. The orange-colored data points in (a) represent the results from the random field approach with $K_y = 60$ fJ/μm^3. All other curves are obtained by considering the thermal distribution of the null-state magnetization.

evolution of the boundary discussed in Fig. 8. The clockwise rotation may expose a more thermally distributed region to the failure part (note the lack of circular symmetry in the contours) that, combined with a longer pulse, could make the relaxation dynamics less stable. Finally, a comparison is made with the results obtained by the conventional random field. As illustrated in Fig. 10(a), both approaches show good agreement for the case of $K_y = 60\ \mathrm{fJ}/\mu\mathrm{cm}^3$. The accuracy beyond 10^{-5} cannot be addressed in the white field treatment due to the limited number of simulation repeats (10^5).

The reliability analysis given above verifies the feasibility of the proposed devices. We can, thus, reasonably set the switching period to 1 ns, with a 0.5-ns TI gate bias followed by a 0.5-ns signal pulse, which is the chosen condition for the one-bit adder simulation (see Sec. IV). The results also indicate a room for further improvement with a total 180° switching period as short as 0.5 ns. The subnanosecond switching time is crucial in achieving low energy consumption, while maintaining sufficient fidelity of operation. In addition, the built-in nonvolatility appears attainable with little or no overhead to the performance specifications. The estimated free-energy barrier of the magnet under discussion ($60 \times 60 \times 2\ \mathrm{nm}^3$, $30\ \mathrm{fJ}/\mu\mathrm{m}^3$) is well over $40k_BT$.

VI. CONCLUSION

The theoretical analysis based on the LLG equation clearly illustrates that the nanomagnet–Dirac-fermion heterostructures provide a unique environment to realize the long-desired goal of inducing and controlling, by electrical means, strongly correlated interactions between electronic and magnetic systems. The proposed device concepts offer a promising alternative in the development of post-CMOS, low-power devices. Further, it is worth noting that application of the spin logic can go beyond the conventional Boolean architecture. With the coupling dependent on the local ensemble of electrons, structures resembling cellular automata and/or a neural network may potentially be achieved as well.

However, numerous challenges are also anticipated for experimental realization as well as more accurate theoretical description. Particularly relevant are the detailed physics at the FM-TI and FM-graphene interfaces that could substantially affect the quantitative picture. While the present treatment is rather heuristic in places relying on the typical parameters in the literature, a more specific consideration may be needed for individual structures. For instance, a recent theoretical study suggests that the coupling between graphene and EuO (a dielectric FM) may induce a sizable, spin-dependent band gap (approximately 100 meV) at the graphene Dirac cone [29]. This large band gap, which could actually be beneficial for large carrier spin polarization just like the quantum confinement gap, appears pertinent only to the material combinations showing good lattice match and proper interfacial configurations [51]. Although EuO is not an ideal FM for the proposed spin logic (due to a low Curie temperature), it, nevertheless, illustrates the complexities of the problem. Experimental demonstration of the device similarly hinges on the high-quality interfaces for strong coupling toward which significant progress is already being made [52]. High material quality is also crucial for minimizing the potential charge or current fluctuations on the TI surface or in the graphene channel, as they could induce corresponding changes in the effective magnetic fields. While small variations within the operating window can be tolerated [see, for example, Figs. 2(b) and 4(c)], the added uncertainties to the device performance may need consideration on top of those of intrinsic thermal origin. A proper circuit design can mitigate the impact at least in part, as well as the progress in the material growth and device fabrication technology.

ACKNOWLEDGMENTS

This work was supported, in part, by the U.S. Army Research Office and FAME (one of six centers of STARnet, a SRC program sponsored by MARCO and DARPA).

[1] D. Chiba, M. Sawicki, Y. Nishitani, Y. Nakatani, F. Matsukura, and H. Ohno, Magnetization vector manipulation by electric fields, Nature (London) **455**, 515 (2008).
[2] K. L. Wang, J. G. Alzate, and P. K. Amiri, Low-power non-volatile spintronic memory: STT-RAM and beyond, J. Phys. D **46**, 074003 (2013).
[3] S. Datta and B. Das, Electronic analog of the electro-optic modulator, Appl. Phys. Lett. **56**, 665 (1990).
[4] J. C. Egues, G. Burkard, and D. Loss, Datta-Das transistor with enhanced spin control, Appl. Phys. Lett. **82**, 2658 (2003).
[5] A. Lyle, S. Patil, J. Harms, B. Glass, X. Yao, D. Lilja, and J. Wang, Magnetic tunnel junction logic architecture for realization of simultaneous computation and communication, IEEE Trans. Magn. **47**, 2970 (2011).
[6] A. Lyle, J. Harms, T. Klein, A. Lentsch, D. Martens, A. Klemm, and J. -P. Wang, Spin transfer torque programming dipole coupled nanomagnet arrays, Appl. Phys. Lett. **100**, 012402 (2012).
[7] D. E. Nikonov, G. I. Bourianoff, and T. Ghani, Proposal of a spin torque majority gate logic, IEEE Electron Device Lett. **32**, 1128 (2011).
[8] H. Dery, P. Dalal, Ł. Cywiński, and L. J. Sham, Spin-based logic in semiconductors for reconfigurable large-scale circuits, Nature (London) **447**, 573 (2007).
[9] B. Behin-Aein, D. Datta, S. Salahuddin, and S. Datta, Proposal for an all-spin logic device with built-in memory, Nat. Nanotechnol. **5**, 266 (2010).
[10] A. Imre, G. Csaba, L. Ji, A. Orlov, G. H. Bernstein, and W. Porod, Majority logic gate for magnetic quantum-dot cellular automata, Science **311**, 205 (2006).
[11] H. Dery, Y. Song, P. Li, and I. Žutić, Silicon spin communication, Appl. Phys. Lett. **99**, 082502 (2011).

[12] S. Rakheja and A. Naeemi, "On physical limits and challenges of interconnects for spin devices," in *Proceedings of the 11th IEEE Conference on Nanotechnology (IEEE-NANO)* (IEEE, Piscataway, NJ, 2011), pp. 1389–1394.

[13] M. T. Niemier, G. H. Bernstein, G. Csaba, A. Dingler, X. S. Hu, S. Kurtz, S. Liu, J. Nahas, W. Porod, M. Siddiq, and E. Varga, Nanomagnet logic: Progress toward system-level integration, J. Phys. Condens. Matter **23**, 493202 (2011).

[14] C. Augustine, G. Panagopoulos, B. Behin-Aein, S. Srinivasan, A. Sarkar, and K. Roy, "Low-power functionality enhanced computation architecture using spin-based devices," in *Proceedings of IEEE/ACM International Symposium on Nanoscale Architecture (NANOARCH)* (IEEE, Piscataway, NJ, 2011), pp. 129–136.

[15] X. Yao, J. Harms, A. Lyle, F. Ebrahimi, Y. Zhang, and J. -P. Wang, Magnetic tunnel junction-based spintronic logic units operated by spin transfer torque, IEEE Trans. Nanotechnol. **11**, 120 (2012).

[16] M. Sharad, C. Augustine, G. Panagopoulos, and K. Roy, Spin-based neuron model with domain-wall magnets as synapse, IEEE Trans. Nanotechnol. **11**, 843 (2012).

[17] H. Dery, H. Wu, B. Ciftcioglu, M. Huang, Y. Song, R. Kawakami, J. Shi, I. Krivorotov, I. Žutić, and L. J. Sham, Nanospintronics based on magnetologic gates, IEEE Trans. Electron Devices **59**, 259 (2012).

[18] D. Pesin and A. H. MacDonald, Spintronics and pseudospintronics in graphene and topological insulators, Nat. Mater. **11**, 409 (2012).

[19] M. Z. Hasan and C. L. Kane, Colloquium: Topological insulators, Rev. Mod. Phys. **82**, 3045 (2010).

[20] W. Han, K. M. McCreary, K. Pi, W. H. Wang, Y. Li, H. Wen, J. R. Chen, and R. K. Kawakami, Spin transport and relaxation in graphene, J. Magn. Magn. Mater. **324**, 369 (2012).

[21] Y. L. Chen, J.-H. Chu, J. G. Analytis, Z. K. Liu, K. Igarashi, H. -H. Kuo, X. L. Qi, S. K. Mo, R. G. Moore, D. H. Lu, M. Hashimoto, T. Sasagawa, S. C. Zhang, I. R. Fisher, Z. Hussain, and Z. X. Shen, Massive Dirac fermion on the surface of a magnetically doped topological insulator, Science **329**, 659 (2010).

[22] X. F. Kou, W. J. Jiang, M. R. Lang, F. X. Xiu, L. He, Y. Wang, Y. Wang, X. X. Yu, A. V. Fedorov, P. Zhang, and K. L. Wang, Magnetically doped semiconducting topological insulators, J. Appl. Phys. **112**, 063912 (2012).

[23] T. Schlenk, M. Bianchi, M. Koleini, A. Eich, O. Pietzsch, T. O. Wehling, T. Frauenheim, A. Balatsky, J. -L. Mi, B. B. Iversen, J. Wiebe, A. A. Khajetoorians, P. Hofmann, and R. Wiesendanger, Controllable magnetic doping of the surface state of a topological insulator, Phys. Rev. Lett. **110**, 126804 (2013).

[24] J. -M. Zhang, W. Zhu, Y. Zhang, D. Xiao, and Y. Yao, Tailoring magnetic doping in the topological insulator Bi_2Se_3, Phys. Rev. Lett. **109**, 266405 (2012).

[25] B. D. Kong, Y. G. Semenov, C. M. Krowne, and K. W. Kim, Unusual magnetoresistance in a topological insulator with a single ferromagnetic barrier, Appl. Phys. Lett. **98**, 243112 (2011).

[26] T. Yokoyama, Current-induced magnetization reversal on the surface of a topological insulator, Phys. Rev. B **84**, 113407 (2011).

[27] J. Linder, Improved domain wall dynamics and magnonic torques via topological insulators, Phys. Rev. B **90**, 041412 (2014).

[28] H. Haugen, D. Huertas-Hernando, and A. Brataas, Spin transport in proximity-induced ferromagnetic graphene, Phys. Rev. B **77**, 115406 (2008).

[29] H. X. Yang, A. Hallal, D. Terrade, X. Waintal, S. Roche, and M. Chshiev, Proximity effects induced in graphene by magnetic insulators: First-principles calculations on spin filtering and exchange-splitting gaps, Phys. Rev. Lett. **110**, 046603 (2013).

[30] A. G. Swartz, P. M. Odenthal, Y. Hao, R. S. Ruoff, and R. K. Kawakami, Integration of the ferromagnetic insulator EuO onto graphene, ACS Nano **6**, 10063 (2012).

[31] X. Duan, V. A. Stephanovich, Y. G. Semenov, and K. W. Kim, Magnetic domain wall transfer via graphene mediated electrostatic control, Appl. Phys. Lett. **101**, 013103 (2012).

[32] H. Ji, J. M. Allred, N. Ni, J. Tao, M. Neupane, A. Wray, S. Xu, M. Z. Hasan, and R. J. Cava, Bulk intergrowth of a topological insulator with a room-temperature ferromagnet, Phys. Rev. B **85**, 165313 (2012).

[33] Y. G. Semenov, X. Duan, and K. W. Kim, Electrically controlled magnetization in ferromagnet-topological insulator heterostructures, Phys. Rev. B **86**, 161406 (2012).

[34] C. H. Bennett, The thermodynamics of computation-a review, Int. J. Theor. Phys. **21**, 905 (1982).

[35] J. Atulasimha and S. Bandyopadhyay, Bennett clocking of nanomagnetic logic using multiferroic single-domain nanomagnets, Appl. Phys. Lett. **97**, 173105 (2010).

[36] A. R. Akhmerov and C. W. J. Beenakker, Boundary conditions for Dirac fermions on a terminated honeycomb lattice, Phys. Rev. B **77**, 085423 (2008).

[37] S. Mandal and S. K. Saha, Ni/graphene/Ni nanostructures for spintronic applications, Nanoscale **4**, 986 (2012).

[38] W. Luo and X.-L. Qi, Massive Dirac surface states in topological insulator/magnetic insulator heterostructures, Phys. Rev. B **87**, 085431 (2013).

[39] Y. G. Semenov, K. W. Kim, and J. M. Zavada, Spin field effect transistor with a graphene channel, Appl. Phys. Lett. **91**, 153105 (2007).

[40] See the corresponding sections of the Supplemental Material at [http://link.aps.org/supplemental/10.1103/PhysRevApplied.2.044003 will be inserted later] for additional details.

[41] S. C. Chan, K. L. Shepard, and P. J. Restle, Distributed differential oscillators for global clock networks, IEEE J. Solid-State Circuits **41**, 2083 (2006).

[42] J. Kiermaier, S. Breitkreutz, I. Eichwald, M. Engelstdter, X. Ju, G. Csaba, D. Schmitt-Landsiedel, and M. Becherer, Information transport in field-coupled nanomagnetic logic devices, J. Appl. Phys. **113**, 17B902 (2013).

[43] D. E. Nikonov and I. A. Young, "Uniform methodology for benchmarking beyond-CMOS logic devices," in *Proceedings of the International Electron Device Meeting* (IEEE, Piscataway, NJ, 2012), pp. 25.4.1–25.4.4.

[44] R. Zhang, K. Walus, W. Wang, and G. A. Jullien, A method of majority logic reduction for quantum cellular automata, IEEE Trans. Nanotechnol. **3**, 443 (2004).

[45] F. Giannazzo, S. Sonde, V. Raineri, and E. Rimini, Screening length and quantum capacitance in graphene by scanning probe microscopy, Nano Lett. **9**, 23 (2009).

[46] G. Bertotti, I. D. Mayergoyz, C. Serpico, and M. d'Aquino, Geometrical analysis of precessional switching and relaxation in uniformly magnetized bodies, IEEE Trans. Magn. **39**, 2501 (2003).

[47] W. F. Brown, Thermal fluctuations of a single-domain particle, Phys. Rev. **130**, 1677 (1963).

[48] I. Cimrák, A survey on the numerics and computations for the Landau-Lifshitz equation of micromagnetism, Arch. Comput. Methods Eng. **15**, 277 (2008).

[49] D. V. Berkov, Fast switching of magnetic nanoparticles: Simulation of thermal noise effects using the Langevin dynamics, IEEE Trans. Magn. **38**, 2489 (2002).

[50] D. V. Berkov, in *Handbook of Magnetism and Advanced Magnetic Materials*, edited by H. Kronmüller and S. Parkin (Wiley, New York, 2007), Vol. 2, pp. 1–29.

[51] P. Lazić, G. M. Sipahi, R. K. Kawakami, and I. Žutić, Graphene spintronics: Spin injection and proximity effects from first principles, Phys. Rev. B **90**, 085429 (2014).

[52] Y. Fan, P. Upadhyaya, X. Kou, M. Lang, S. Takei, Z. Wang, J. Tang, L. He, L.-T. Chang, M. Montazeri, G. Yu, W. Jiang, T. Nie, R. N. Schwartz, Y. Tserkovnyak, and K. L. Wang, Magnetization switching through giant spin-orbit torque in a magnetically doped topological insulator heterostructure, Nat. Mater. **13**, 699 (2014).